nature photonics

Article

https://doi.org/10.1038/s41566-022-01129-1

Terahertz cyclotron emission from two-dimensional Dirac fermions

In the format provided by the authors and unedited

Table of Contents

Low-energy BHZ Hamiltonian for Dirac fermions in HgTe quantum wells *2*
Transport characterization *4*
Temperature influence on the cyclotron resonance energy *5*
Cyclotron emission obtained in a wide gapless QW *7*
Influence of the applied voltage on the emission amplitude and absence of correlation between the emission drop and the magnetoresistance *8*
Incipient Landau quantization regime *9*
Recombination processes and population inversion *10*
Figure and table for Methods *11*

Low-energy BHZ Hamiltonian for Dirac fermions in HgTe quantum wells

The low-energy band structure in HgTe QWs in the vicinity of the Γ point of the Brillouin zone is analytically described within the Dirac-like Bernevig-Hughes-Zhang (BHZ) model [1]. This model takes into account the lowest electron-like level $E1$, formed by the Bloch functions at the Γ point of the Brillouin zone with the total angular momentum $m_J=\pm 1/2$, and the top hole-like level $H1$ formed by the Bloch functions of heavy-holes with $m_J=\pm 3/2$ [1]. In the basis $|E1,+\rangle$, $|H1,+\rangle$, $|E1,-\rangle$, $|H1,-\rangle$, the BHZ Hamiltonian is written as

$$H_{\mathrm{BHZ}}(\mathbf{k}) = \begin{pmatrix} H_+(\mathbf{k}) & 0 \\ 0 & H_-(\mathbf{k}) \end{pmatrix}, \tag{SM1}$$

where $\mathbf{k} = (k_x, k_y)$ is the momentum in the QW plane, and

$$H_+(\mathbf{k}) = (C - \mathbb{D}k^2)\sigma_0 + (M - \mathbb{B}k^2)\sigma_z + A\left(k_x\sigma_x + k_y\sigma_y\right). \tag{SM2}$$

Here, σ_0 is a 2×2 unit matrix, namely I_2, σ_α (with α=x, y or z) are the Pauli matrices, and C, M, A, $\mathbb{B}$, $\mathbb{D}$ are the structure parameters, which depend on the QW width, the barrier material, the QW growth direction and external conditions [2], respectively. The mass parameter M defines the band gap (which equals $2M$) at the Γ point ($\mathbf{k} = 0$) and the ordering of $E1$ and $H1$ subbands. For instance, the electron-like subband lies below the hole-like at $M < 0$. The blocks $H_+(\mathbf{k})$ and $H_-(\mathbf{k})$ in Eq. (1) describe the spin-up and spin-down electrons in the $E1$ and $H1$ subbands, respectively. Note that due to time reversal-symmetry $H_-(\mathbf{k}) = H_+^*(-\mathbf{k})$, where the star represents the complex conjugation. In Eq. (1), we have also neglected the small terms breaking inversion [3] and axial symmetries [4] around the growth direction, which results in the block-diagonal form of $H_{\mathrm{BHZ}}(\mathbf{k})$.

The terms $\mathbb{D}k^2\sigma_0$ and $\mathbb{B}k^2\sigma_z$ in Eq. (SM2) quadratic in momentum are not present in the Dirac Hamiltonian familiar from relativistic quantum mechanics, but they play an important role in semiconductor QWs. In particular, the relative sign of $\mathbb{B}$ and M determines the Z_2 classification: the system is classified as a topologically trivial insulator if $M\mathbb{B} < 0$ and non-trivial insulator for $M\mathbb{B} > 0$ [1]. Since for HgTe QWs $\mathbb{B} < 0$, the inverted QW with $M < 0$ is thus a non-trivial topological insulator (for Fermi energies inside the gap), while the non-inverted QW with $M > 0$ is a trivial band insulator. The phase transition between these two types of insulators therefore occurs at $M = 0$, when the QW band structure mimics massless Dirac fermions.

The Hamiltonian (SM1) can be exactly diagonalized, and the two branches of doubly degenerated eigen-energies are:

$$E_s^{(\pm)}(\mathbf{k}) = C - \mathbb{D}k^2 + s\sqrt{(M - \mathbb{B}k^2)^2 + A^2k^2}, \tag{SM3}$$

where $s = +1$ (-1) stands for the conduction (valence) band, and the superscript ± of $E_s^{(\pm)}(\mathbf{k})$ stands for spin up (down) component, which are degenerated here.

To calculate Landau levels (LLs) dispersion in the presence of an external magnetic field $\boldsymbol{B}$ oriented perpendicular to the QW plane, one should make the Peierls substitution of the momentum $\mathbf{k} \to -i\boldsymbol{\nabla} + e\mathbf{A}/c\hbar$ (where $\mathbf{A}$ is the vector potential so that $\boldsymbol{B} = \boldsymbol{\nabla} \times \mathbf{A}$) and add an additional Zeeman term H_{Z} to $H_{\mathrm{BHZ}}(\mathbf{k})$

$$H_Z = \frac{\mu_B B}{2}\begin{pmatrix} g_e & 0 & 0 & 0 \\ 0 & g_h & 0 & 0 \\ 0 & 0 & -g_e & 0 \\ 0 & 0 & 0 & -g_h \end{pmatrix}. \tag{SM4}$$

Here, μ_B is the Bohr magneton, and g_e and g_h are the g-factors describing the Zeeman splitting in $E1$ and $H1$ subbands, respectively. Solving the eigenvalue problem in the presence of magnetic field, the LL energies are found analytically [5]:

$$E_{n\geq 1}^{(\pm)} = C - \frac{2\mathbb{D}n \pm \mathbb{B}}{a_B^2} \pm \frac{g_e + g_h}{4}\mu_B B + s\sqrt{\left(M - \frac{2\mathbb{B}n \pm \mathbb{D}}{a_B^2} \pm \frac{g_e - g_h}{4}\mu_B B\right)^2 + \frac{2nA^2}{a_B^2}},$$

$$E_0^{(+)} = C + M - \frac{\mathbb{D}+\mathbb{B}}{a_B^2} + \frac{g_e}{2}\mu_B B,$$
$$E_0^{(-)} = C - M - \frac{\mathbb{D}-\mathbb{B}}{a_B^2} - \frac{g_h}{2}\mu_B B, \quad \text{(SM5)}$$

where a_B is the magnetic length ($a_B^2 = c\hbar/eB$). Typically in HgTe $g_e \gg g_h$ [6], so the latter can be neglected.

As mentioned in the main text, the most essential difference between massless Dirac Fermions in semiconductor QWs and those in graphene is the absence of spin degeneracy of the LLs due to non-zero values of $\mathbb{B}$, $\mathbb{D}$, g_e and g_h. These terms also result in the absence of the series of equidistantly spaced LLs, as existing in graphene. In order to calculate the structure parameters for the BHZ Hamiltonian, we apply the perturbative approach [7] to the 8-band **k·p** Hamiltonian [8]. This model directly takes into account the interactions between Γ_6, Γ_8 and Γ_7 bands in bulk materials and well describes the electronic states in HgCdTe-based QWs. In the 8-band Kane Hamiltonian, we take into account the terms, describing the strain effect arising due to mismatch of lattice constants in the buffer, QW layers and CdHgTe barriers [8]. Parameters for the bulk materials, and valence band offsets, used in the 8-band Kane model, are taken from Ref [8]. In the main text, we consider the QWs, grown along (001) and (013) crystallographic orientations.

To derive effective 2D BHZ Hamiltonian valid in the vicinity of the Γ point from the 8-band Kane model, we follow the procedure proposed in Ref. [9] and described in details in the supplementary materials of Ref. [7]. First, we split the Kane Hamiltonian H^{Kane} into two parts $\boldsymbol{H}^{Kane} = \boldsymbol{H}^{(0)}(k_z) + \boldsymbol{H}^{(1)}(k_z, k_x, k_y)$, where $\boldsymbol{H}^{(0)}(k_z)$ is the Kane Hamiltonian at $k_x = k_y = 0$. In our case, the *z* axis is oriented along (0*mn*) direction (*m* and *n* are positive integer), while the *x* and *y* axes correspond to the directions (100) and $(0n\bar{m})$, respectively. Then, we numerically diagonalize $\boldsymbol{H}^{(0)}(k_z)$, to obtain the energies and envelope functions and to classify of electronic levels as electron-like *Ep*, hole-heavy-like *Hn*, light-hole-like *LHp* or spin-off-like *SOp* levels (p = 1, 2, …). After, we group the eigenstates of $\boldsymbol{H}^{(0)}(k_z)$ into *A* and *B* subsets. The *A* subset includes the basis states of $\{|E1,\pm\rangle, |H1,\pm\rangle\}$ levels. In the *B* subset, we consider eight above-lying electron-like states and eight subbands for light-hole-like and hole-heavy-like states. All the other subbands are neglected since they are well separated in energy. The states in both classes are not coupled, since they are eigenstates of $\boldsymbol{H}^{(0)}(k_z)$. The presence of $\boldsymbol{H}^{(1)}(k_z, k_x, k_y)$ introduces the mixing between the states from two subsets. To derive effective BHZ Hamiltonian, we treat $H^{(1)}(k_z, k_x, k_y)$ as a small perturbation and apply the second-order Löwdin perturbation method to eliminate the coupling between the states from different subsets [9]:

$$H_{\mathrm{BHZ}}(\mathbf{k})_{m,m'} = E_m\delta_{m,m'} + H^{(1)}_{m,m'} + \frac{1}{2}\sum_l H^{(1)}_{m,l}H^{(1)}_{l,m'}\left(\frac{1}{E_m - E_l} + \frac{1}{E_{m'} - E_l}\right). \quad \text{(SM6)}$$

Here, the indices *m*, *m'* correspond to states in set *A*, the indices *l* correspond to the states in set *B*, $H^{(1)}_{m,m'}$ is the matrix element of $\boldsymbol{H}^{(1)}(k_z, k_x, k_y)$, calculated by using the envelope function of $\boldsymbol{H}^{(0)}(k_z)$. Parameters for BHZ Hamiltonian calculated for different thicknesses of HgTe QWs are provided in Table SM1. Figure SM1 shows the band dispersion for gapless and inverted HgTe/$Cd_{0.7}Hg_{0.3}$Te QWs grown on (013) CdTe buffer (see Tab. SM1). One can see, that for small values of the wave vector, the energy dispersion is reproduced by both the BHZ and 8-band **k·p** models. The two models show significant deviations at higher **k** values.

Table SM1. Structure parameters involved in the BHZ Hamiltonian for HgTe/Cd_xHg_{1-x}Te QWs grown on (013)-oriented CdTe buffer, which were used for the calculations presented in Fig. 1 and 3 in the main text.

d (nm)	x	C (meV)	M (meV)	A, (meV·nm)	$\mathbb{B}$ (meV·nm^2)	$\mathbb{D}$ (meV·nm^2)	g_e	g_h
6.2	0.65	–26.5	0	375.8	–634.4	–451.6	59.15	2.43
8	0.8	–32.8	–12.7	353.3	–828.5	–645.4	44.04	2.41

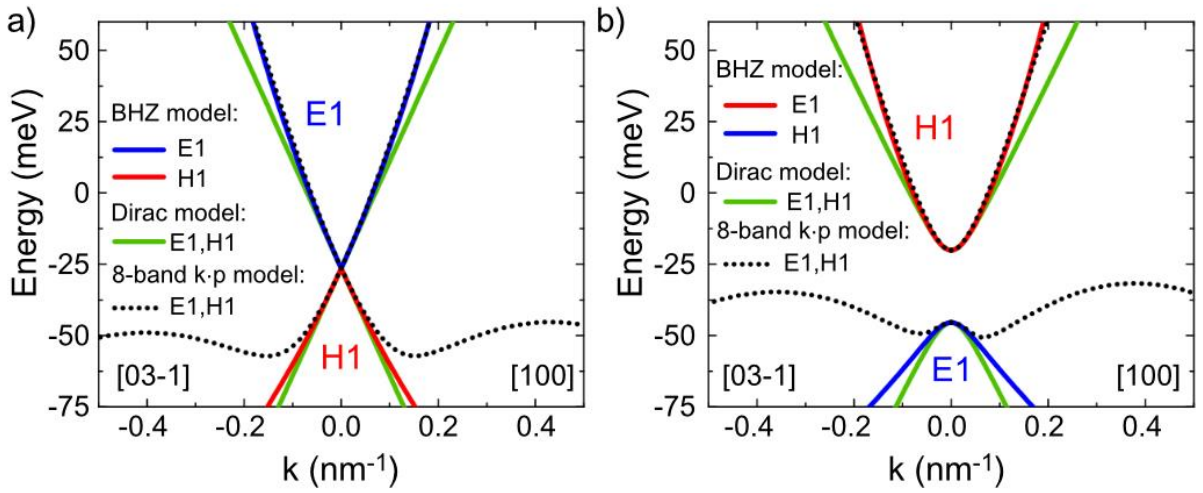

Figure SM1: Comparison of energy dispersion for a) gapless HgTe/$Cd_{0.65}Hg_{0.35}$Te QWs and b) gapped HgTe/$Cd_{0.8}Hg_{0.2}$Te QWs calculated on the basis of the BHZ and 8-band **k·p** models. To stress the role of the quadratic terms, the green curves also represent the band structure within the Dirac model, i.e. the BHZ Hamiltonian at $\mathbb{B} = \mathbb{D} = 0$. It is noticeable, that for small values of **k**, all models reproduce the same behavior while for higher **k** a significant deviation may arise.

Transport characterization

All the samples studied for emission in this paper were additionally characterized by means of magneto-transport as it is presented on Figure SM 2 for the single 8nm thick quantum well sample #101109. The carriers' concentration was calculated from the period of Shubnikov-de-Haas oscillations in reciprocal magnetic field, $N = 4.58 \cdot 10^{11}$ cm^{-2}. Then, Van der Pauw method was employed to determine the carriers' mobility: a four-point probe placed around the perimeter of the sample allows measuring the average conductivity of the sample at liquid helium temperature. For instance, for the sample #101109 the conductivity $\sigma = 0.0113146$ Ohm·m. Finally, knowing the carrier's concentration in the sample and the conductivity one may calculate the mobility: $\mu = 154000$ cm^2/V·s. All these data are presented in the summary table in the main text.

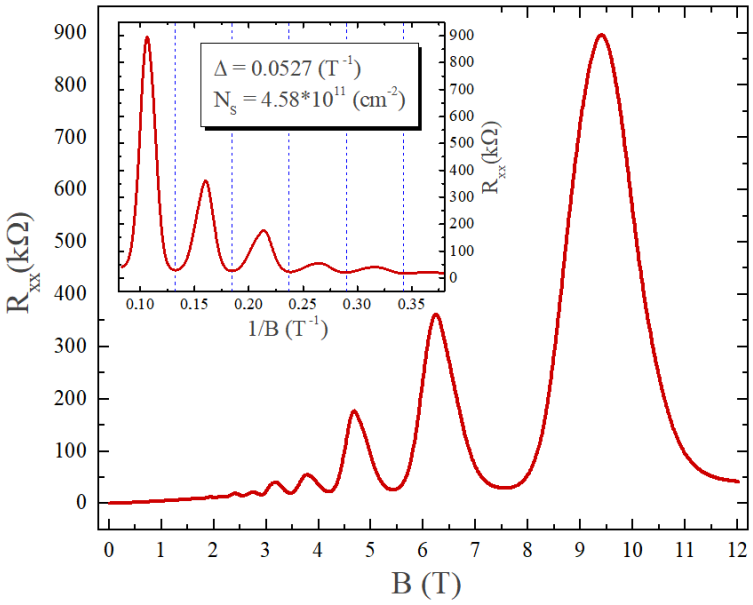

Figure SM2: The longitudinal magneto-transport curve of the single 8 nm QW exhibits nicely seen Shubnikov-de Haas oscillations. The figure inset shows these oscillations in the reciprocal magnetic field, their period in 1/B allows to determine the sheet density of the carriers $N_S = e/\Delta h = 4.58 \cdot 10^{11}$ cm^{-2}.

Temperature influence on the cyclotron resonance energy

It is well known that temperature has a significant influence on the band structure of HgCdTe compounds. This can even be used to induce a topological phase transition at the critical temperature T_c[10]. Thus, when considering radiative transitions between discrete LLs, the change of temperature can significantly influence the emission energy. Here, due to the different nature of the emission, originating from the quasi-classical cyclotron resonance, the influence of temperature on the emission frequency should be negligible. To verify this, we studied additional to the emission spectra, the transmission spectra for one sample as illustrated in Ref [10] (sample named 091222 in this reference). The comparison between these two methods, in the same sample at a given magnetic field value, is shown in Figure SM3. The upper part shows the emission spectra obtained at 4.2 K while the lower part shows the transmission spectra for different temperatures ranging from 2 K to 100 K, with a fixed magnetic field B_{sample} = 2 T for all measurements. Comparing the transmission measurements at different temperatures it is obvious that the absorption energy does not change and the slight decrease in amplitude may be associated with the reduced sensibility of the bolometer at elevated temperatures. We note that there is a slight difference between the emission and absorption energy. This can stem from deviations in the quantum well thickness or in the Cd content in the barriers even when using samples from the same wafer. However, these results seem to confirm the possibility of observing a cyclotron emission at temperatures reachable by Peltier coolers, without significant variation in the emission frequency.

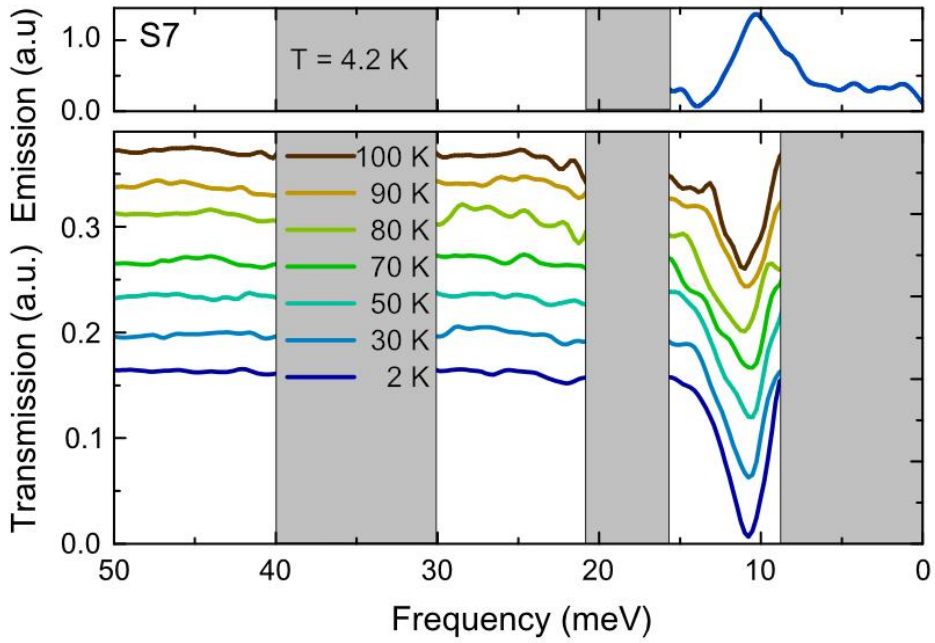

Figure SM3: Comparison of the emission (upper part) and absorption (lower part) spectra of an 8nm QW (Sample 091222) at a fixed magnetic field of 2T. The absorption was measured at different temperatures ranging from 2 K to 100 K.

Furthermore, it might not be sufficient to only consider one chosen magnetic field, since in the crossed fields configuration the general behaviour of the emission line may change even when the energy at a fixed magnetic field doesn't change. In Figure SM4 we therefore show an extended dependence with multiple absorption and emission measurements at different magnetic fields and temperatures ranging from 2 K to 130 K. The solid lines indicate calculated LL transition energies in accordance to Ref. [10]. Stars are absorption peak maxima extracted from the measurements as shown in Figure SM3. Full and empty circles are emission peaks maxima obtained in the two different operation modes of the emission setup, i.e. with fixed detector energy or fixed B_{sample}, where the FWHM of latter measurements is shown as error bars. The dashed green line is the emission line obtained at 4.2 K. One can see, that temperature independence assumed from Figure SM3, is indeed true for multiple magnetic field in the temperature range of almost 130 K.

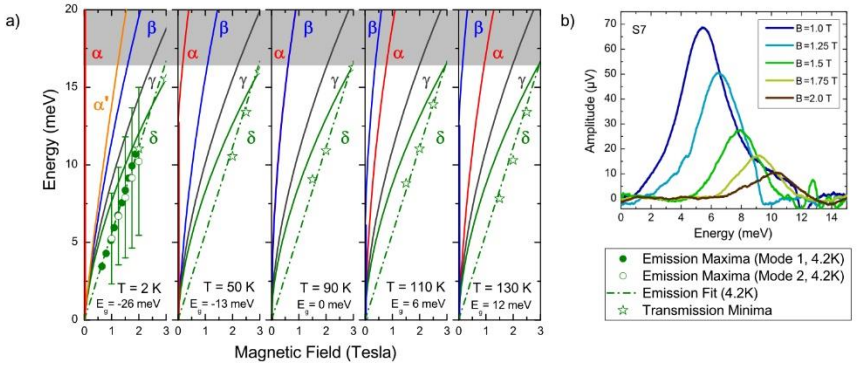

Figure SM4: a) Comparison of the emission and absorption spectra for an 8nm QW (Sample 091222) at different magnetic fields and temperatures, ranging from 2 K to 130 K. Solid lines indicate calculated LL transition energies. Stars are absorption peak maxima extracted from the measurements as shown in Figure SM3. Full end empty circles are emission peaks maxima obtained in the two different operation modes of the emission setup, i.e. with fixed detector energy or fixed B_{sample}, where the FWHM of latter measurements is shown as error bars. The dashed line indicates the emission spectra obtained at 4.2K.

b) Full emission spectra of an 8nm QW (Sample 091222) at 4.2 K and different magnetic fields as indicated in panel a).

Cyclotron emission obtained in a wide gapless QW

For typical gapless HgTe/CdTe QWs the well thickness is close to critical (6.3 nm). However, this is only true if the QW consists of pure HgTe. This changes when Cd is added to the well. In this case the gapless state and its associated Dirac cone are reproduced for much higher thicknesses. For a Cd concentration of 13.9%, the gapless state is realized at a thickness of 30 nm. The schematic layer structure of such a sample studied in emission is shown in Figure SM5 b). The corresponding energy spectra obtained for different fixed magnetic fields is shown next to it (Figure SM5 a). We emphasize, that so far this was the sample with the highest tuneability (~5THz/T) reaching almost the record value of gapless $Hg_xCd_{1-x}Te$ bulk films (6THz/T).

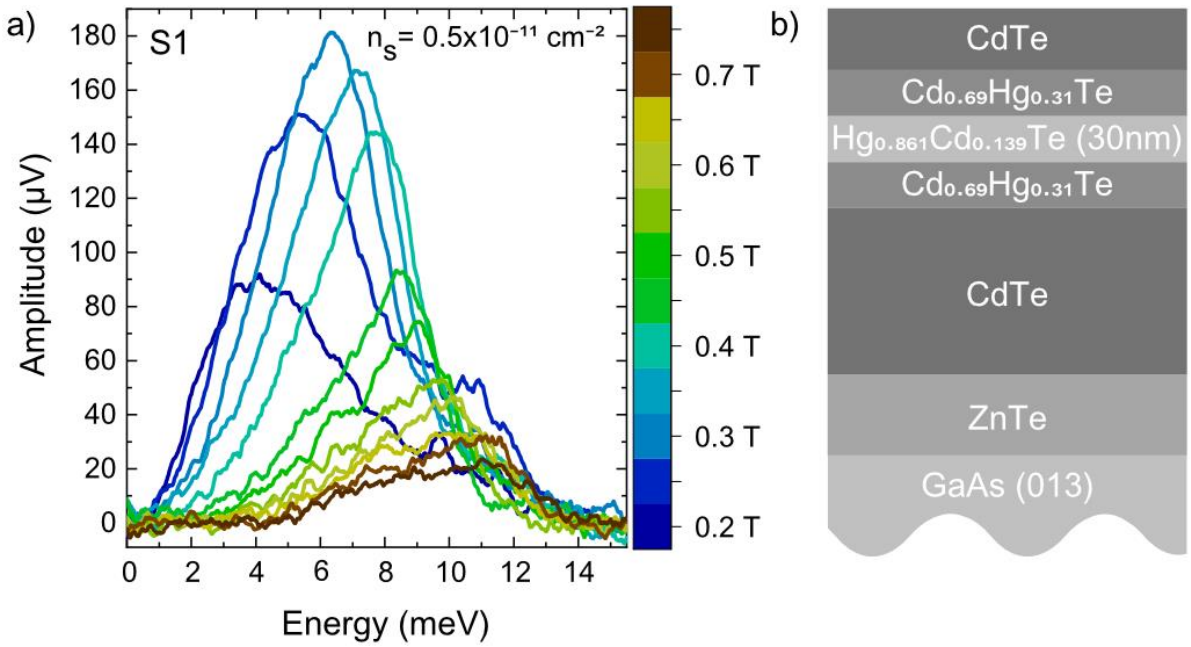

Figure SM5: a) Emission Spectra obtained with the sample S1, a gapless 30nm thick QW with 13.9% Cd in the QW. The corresponding layer structure is schematically shown in b)

Influence of the applied voltage on the emission amplitude and absence of correlation between the emission drop and the magnetoresistance

It is clear that the amplitude of the cyclotron emission increases with the applied voltage (see side peaks at the finite values of B in the Figure below). The best conditions for observing the emission in this sample were obtained with a voltage of 12 V applied between the contacts. In all the measurements made with the different samples, we tried to use conditions in which the cyclotron emission was most pronounced and the thermal background still relatively low so that the background noise could be easily subtracted. It should be mentioned that even though measurement at higher voltages and reduced duty cycle was possible, the risk of damaging the sample or destroying the gold wires at zero magnetic field was rather high. It was therefore better to find a compromise and use lower voltages most of the time.

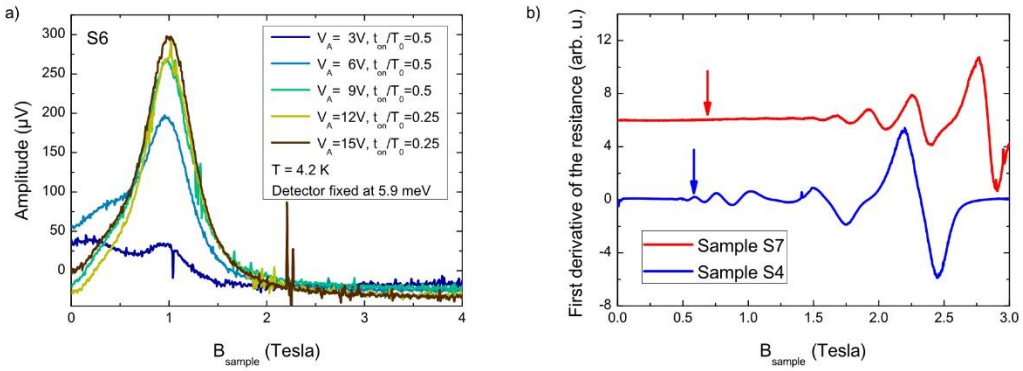

Figure SM6: a) Emission spectra measured in sample S6 at different applied voltages and duty cycles. b) The first derivative of the magnetoresistance at low magnetic field measured at 4K in samples S4 and S7. The black arrows represent the magnetic field at which the emission signal drops in each samples.

The decrease in amplitude of the cyclotron emission observed systematically in all our samples could also have been attributed to the non-linearities of resistance in the magnetic field. In this case, one would expect to observe a change in the resistance to the magnetic field at which the emission amplitude decreases. The following figure therefore shows two examples of first derivatives of the magnetoresistance of these samples in order to highlight a possible correlation between the signal drop (whose corresponding magnetic fields are represented by the black arrows), and a nonlinearity of the magnetoresistance. This correlation is not observed in these two samples and therefore this decrease cannot be attributed to such an effect, nor to the appearance of Shubnikov-de Haas oscillations.

Incipient Landau quantization regime

The notion of discreteness of LLs is crucial in the context of the cyclotron emission in HgTe QWs, as for suppressing Auger recombination, LLs must be separated. However, the samples are neither into the quantized regime in which the LLs are totally separated (i.e. the energy gap between LLs is greater than their broadening), nor in the quasi-classical regime in which the LLs form a quasi-continuum of energy. They are indeed in conditions of *incipient* quantization, as introduced for example in [11,12,13,14,15]. In this intermediate regime the LLs are already defined, but given their width, they partially overlap (i.e. the energy gap between LLs is smaller than their broadening). The "*incipient* Landau quantization" regime is defined by the region of magnetic field between $\omega_c\tau_t \sim 1$, where τ_t is the transport scattering time, and $\omega_c\tau_q \sim 1$, where τ_q is the quantum scattering time, which is the average time an electron stays in a given quantum state [16]. Note that τ_q is directly connected with the collision broadening of the Landau levels [17]. It is determined by fitting the envelope of Shubnikov-de Haas (SdH) oscillations at quantizing magnetic fields [18,19]. In the regime of our cyclotron emission experiments, we do already observe SdH oscillations in the magneto-resistance. This indicates that the LLs are *de facto* separated. At the same time, several emission modes contribute to the observed cyclotron emission. Each of them necessarily follows the √B dependence, imprinted by the emerging LL quantization, nevertheless, their envelope still evolves rather linearly with B. Analogous behavior was observed, for instance, in high-field cyclotron resonance experiments on doped graphene, see [20].

The figure below illustrates the incipient regime. The magnetic field at which $\omega_c\tau_q = 1$ is $B_q = 2.25$ T (Fig. SM8) in the sample S7. For the extraction of the quantum time ($\tau_q = 5.10^{-14}$ s), we used the formula: $\Delta\rho_{xx} = 4\,\rho_0 \exp(-\pi/\mu_q B)$ to fit the SdH peak amplitude, where the quantum mobility is given as $\mu_q = e\,\tau_q/m^*$, and ρ_0 is the resistivity at B0.

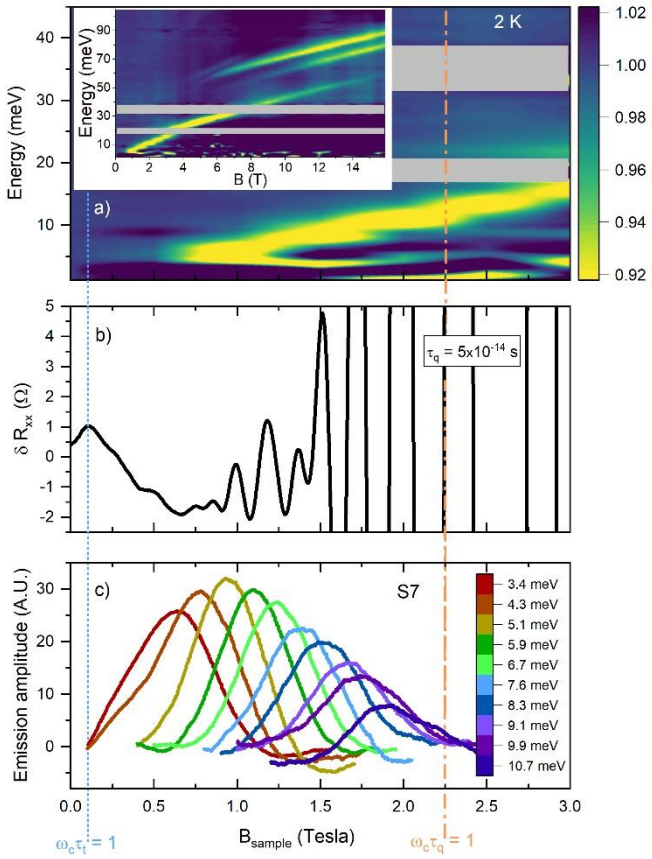

Figure SM7: Illustration of the incipient regime in sample S7. The quasi-classical regime, represented by the region below the vertical dotted line, is defined by $\omega_c\tau_t < 1$, where ω_c is the cyclotron frequency and τ_t is the transport scattering time determined from low magnetic field measurements using the Drude model from the Hall mobility ($\mu = e\tau/m^*$). The regime of incipient quantization of the LLs is between $\omega_c\tau_t \sim 1$ (represented by the vertical dotted line) and $\omega_c\tau_q \sim 1$ (represented by the vertical dashed line) where τ_q is the quantum scattering time extracted from the envelope of SdH oscillations and defining the broadening of Landau levels. Note however that $\omega_c\tau_q \sim 1$ as upper bound of the incipient regime is not a strict condition but rather an estimate. a) Magneto-absorption results measured in sample S7 in the form of a color map. The cyclotron resonance evolves linearly with magnetic field up to approximately 3 T. Full LL mapping is provided in the insert to visualize the difference between low field and high field optical transitions. At high magnetic fields (above 4 T), the sample is in the quantum regime, and unlike in the low field region, the energy evolution of inter-LL transitions becomes nonlinear. However, as shown in panel b), SdH oscillations are already visible from a magnetic field of 0.7 T, i.e. between $\omega_c\tau_t \sim 1$ and $\omega_c\tau_q \sim 1$, c) Cyclotron emission at different detection energies clearly appears in the incipient quantization regime.

Recombination processes and population inversion

Regarding the population inversion, the following 3 key conditions are met: i) there is Landau quantization, though LLs partially overlap; ii) there is a population inversion, i.e. the population of some LL (n) is greater than in the lower one (n-1); iii) the system is nonparabolic, i.e. the distance between (n+1) and (n) LLs is smaller than between (n) and (n-1) ones. In these conditions, let us consider if the nonradiative Auger recombination can kill the population inversion (the latter is the necessary condition for stimulated cyclotron emission). If an electron from the (inversely populated) n^{th} LL recombine

nonradiatively to the $(n-1)^{th}$ LL, its energy must be transferred to another electron. If this other electron also occupies the $(n-1)^{th}$ LL, it is then excited and returns to the n^{th} LL. In this case nothing has changed. On the other hand, if this other electron, to which the energy has been transferred, occupies a LL lower than the $(n-1)^{th}$, non-parabolicity implies (due to the energy conservation law) that non-radiative recombination takes place towards the DOS tail of this lower LL and its probability is therefore reduced. Thus, non-parabolicity reduces both the Auger recombination probability and the absorption probability of light between the n^{th} and the $(n+1)^{th}$ LL emitted during the radiative transition of the n^{th} to the $(n-1)^{th}$ LL.

Figure and table for Methods

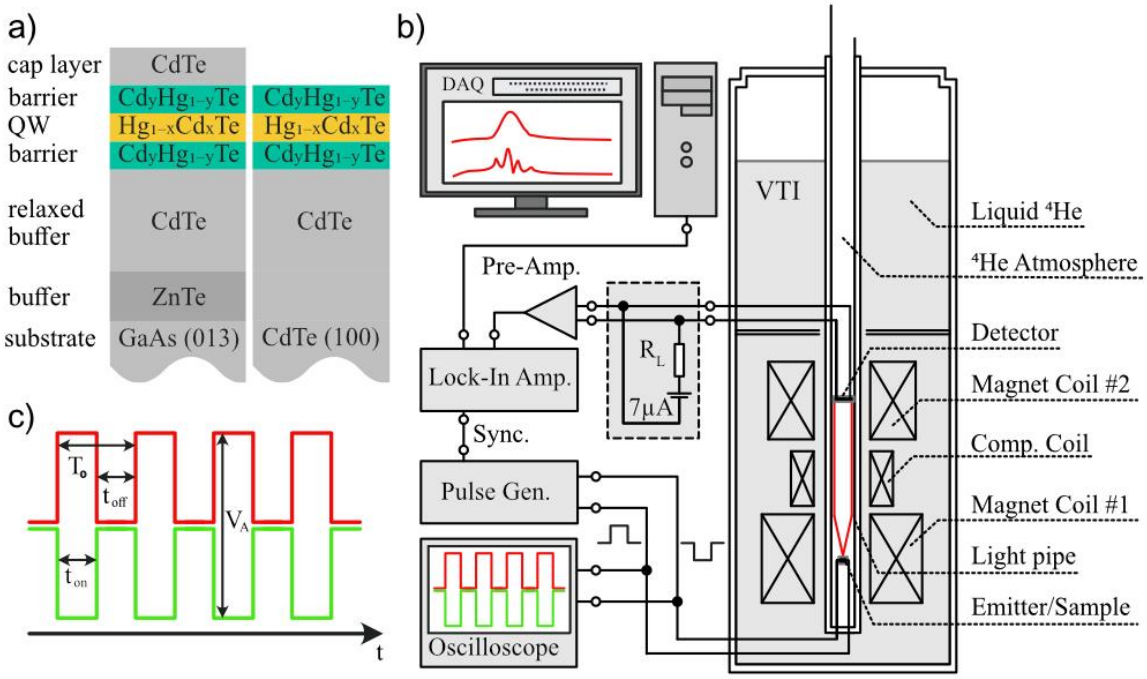

Fig. SM8: Description of the Landau spectroscopy experimental setup. a) The samples are HgCdTe/CdHgTe QWs of different thicknesses and Cd compositions, on GaAs and CdTe substrates. b) The spectrometer is integrated in a cryostat and composed of two superconducting coils. One of them allows to apply a magnetic field to the measured sample while the other is applied to the cyclotron detector. A weaker third coil makes it possible to compensate for the action of the first on the second. The sample is excited by electrical pulses and the duty cycle of a few percent, detailed in c), is generally set to prevent overheating of the sample. The Landau emission signal is finally detected as a voltage drop across the InSb detector which is then amplified and measured via a standard lock-in technique.

Sample	Wafer	QW width (nm)	Gap width (meV)	Number of QWs	Carrier density $*10^{11}$ (cm^{-2})	Carrier mobility (cm^2/Vs)	Cyclotron mass m_c/m_e	FWHM (meV)	Collision broadening (meV)
S9	**130415**	6.3	~ 0	1	1.3	130 000	0.01249	-	0.71
S5	**101227**	6.5	~ 0	1	1.6	225 000	0.01433	-	0.36
S7	**091222-1**	8	28.1	1	3.1	190 000	0.02082	3.27	0.29
S6	**091223-1**	8	30.4	1	1.95	205 000	0.01855	2.51	0.30
S8	**101109**	8	-	1	4.58	154 000	0.02463	3.11	0.30
S2	**210702-5**	8.5	25-30	15	0.83	115 000	0.00788	-	1.27
S3	**170410**	8.0-8.2	-	50	0.23	80 000	0.00899	-	1.60

S1	**091225**	30	~ 0	1	0.5	105 000	0.0055	4.86	2
S4	**28104**	8	-	1	0.6	185 000	0.0125	3.58	0.5

Table SM2: Parameters summary for the samples presented in this work. Carrier density and mobility are extracted from transport measurements (see supplementary information); other parameters are extracted from the emission data.

[1] B.A. Bernevig, T.L. Hughes, and S.-C. Zhang, Science **314**, 1757 (2006).

[2] S. S. Krishtopenko, I. Yahniuk, D. B. But, V. I. Gavrilenko, W. Knap, and F. Teppe, Phys. Rev. B **94**, 245402 (2016)

[3] M. Konig, H. Buhmann, L. W. Molenkamp, T. Hughes, C.-X. Liu, X.-L. Qi, and S.-C. Zhang, J. Phys. Soc. Jpn. **77**, 031007 (2008).

[4] D. G. Rothe, R. W. Reinthaler, C.-X. Liu, L. W. Molenkamp, S.-C. Zhang, and E. M. Hankiewicz, New J. Phys. **12**, 065012 (2010).

[5] M. König, S. Wiedmann, C. Brüne, A. Roth, H. Buhmann, L. W. Molenkamp, X.-L. Qi, and S.-C. Zhang, Science **318**, 766 (2007).

[6] A.M. Kadykov, S.S. Krishtopenko, B. Jouault, W. Desrat, W. Knap, S. Ruffenach, C. Consejo, J. Torres, S.V. Morozov, N.N. Mikhailov, S.A. Dvoretskii, and F. Teppe, Phys. Rev. Lett. **120**, 086401 (2018).

[7] S.S. Krishtopenko, W. Knap, and F. Teppe, Sci. Rep. **6**, 30755 (2016).

[8] S.S. Krishtopenko, I. Yahniuk, D.B. But, V.I. Gavrilenko, W. Knap, and F. Teppe, Phys. Rev. B **94**, 245402 (2016).

[9] D.G. Rothe, R.W. Reinthaler, C.-X. Liu, L.W. Molenkamp, S.-C. Zhang, and E.M. Hankiewicz, New J. Phys. **12**, 065012 (2010).

[10] M. Marcinkiewicz, S. Ruffenach, S.S. Krishtopenko, A.M. Kadykov, C. Consejo, D.B. But, W. Desrat, W. Knap, J. Torres, A.V. Ikonnikov, K.E. Spirin, S.V. Morozov, V.I. Gavrilenko, N.N. Mikhailov, S.A. Dvoretskii, and F. Teppe, Phys. Rev. B. **96**, 035405 (2017).

[11] P. Plochocka, P. Kossacki, A. Golnik, T. Kazimierczuk, C. Berger, W. A. de Heer, and M. Potemski, Phys. Rev. B **80**, 245415 (2009)

[12] L. A. Ponomarenko, R. Yang, R. V. Gorbachev, P. Blake, A. S. Mayorov, K. S. Novoselov, M. I. Katsnelson, and A. K. Geim, Phys. Rev. Lett. **105**, 136801 (2010)

[13] H. Ramamoorthy, R. Somphonsane, G. He, D. K. Ferry, Y. Ochiai, N. Aoki and J. P. Bird, Appl. Phys. Lett. **104**, 193115 (2014); https://doi.org/10.1063/1.4878535

[14] G. Ferrari, A. Bertoni, G. Goldoni, and E. Molinari, Phys. Rev. B **78**, 115326 (2008)

[15] S. Bhat, J.S. Bhat, Solid State Communications **346**, 114709, (2022)

[16] M. Sakowicz, J. Łusakowski, K. Karpierz, M. Grynberg, and B. Majkusiak, Applied Physics Letters 90, 172104 (2007); doi: 10.1063/1.2731713

[17] J. P. Harrang, R. J. Higgins, R. K. Goodall, P. R. Jay, M. Laviron, and P. Delescluse, Phys. Rev. B **32**, 8126 (1985)

[18] P. Lorenzini, Z. Bougrioua, A. Tiberj, R. Tauk, M. Azize, M. Sakowicz, K. Karpierz, and W. Knap, Appl. Phys. Lett. **87**, 232107 (2005); doi: 10.1063/1.2140880

[19] P. T. Coleridge, R. Stoner, R. Fletcher, Phys. Rev. B **39**, 1120 (1989)

[20] M. Orlita, I. Crassee, C. Faugeras, A. B. Kuzmenko, F. Fromm, M. Ostler, Th. Seyller, G. Martinez, M. Polini and M. Potemski, New J. Phys. **14**, 095008 (2012)